Mann, T., et al., 2023, Fossil Java Sea corals record Laurentide ice sheet disappearance: Geology, https://doi.org/10.1130/G51038.1

# Supplemental Material

**Figures S1–S8**

**Table S1–S3**

**Supplemental Text**

**Supplemental Material for „ Fossil Java Sea corals record Laurentide ice sheet disappearance" by Mann et al.**

## 1. Information on cyclone activity in the Java Sea

The Southern Hemisphere Tropical Cyclone Data Portal of the Australian Bureau of Meteorology contains no records of tropical cyclone activity since the 1969/70 cyclone season on the Sunda Shelf and in the Java Sea (Supplemental Figure S1).

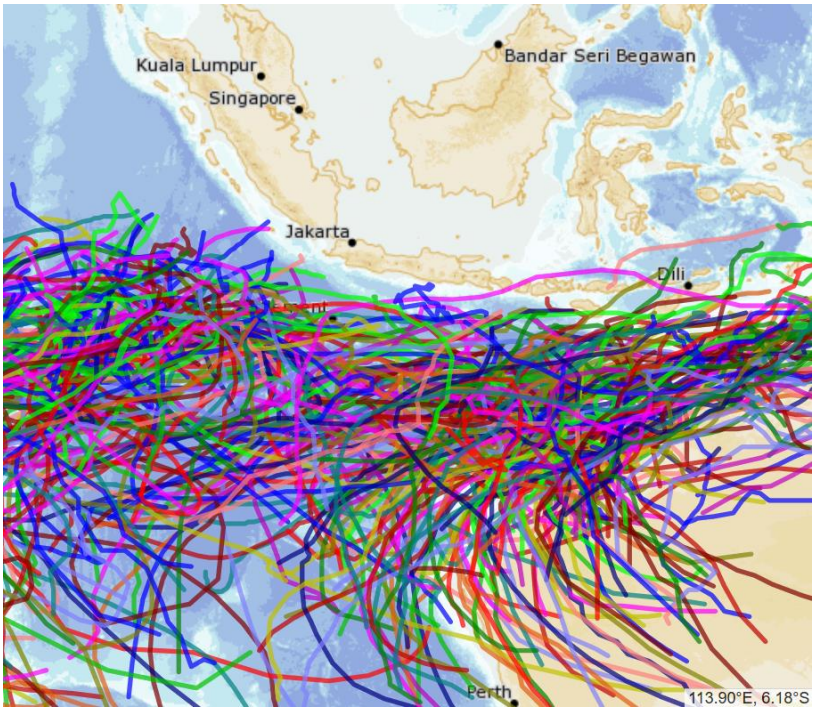


**Supplemental Figure S1:** Cyclone tracks since 1969/1970 in the region around the Java Sea (from http://www.bom.gov.au/cyclone/tropical-cyclone-knowledge-centre/history/tracks/)

## 2. Information on earthquake occurrences in the Java Sea

The earthquake database from the United States Geological Survey contains no records of shallow (0 – 33 km) earthquakes close to the study site that could cause a vertical displacement of the crust at the surface (Supplemental Figure S2).

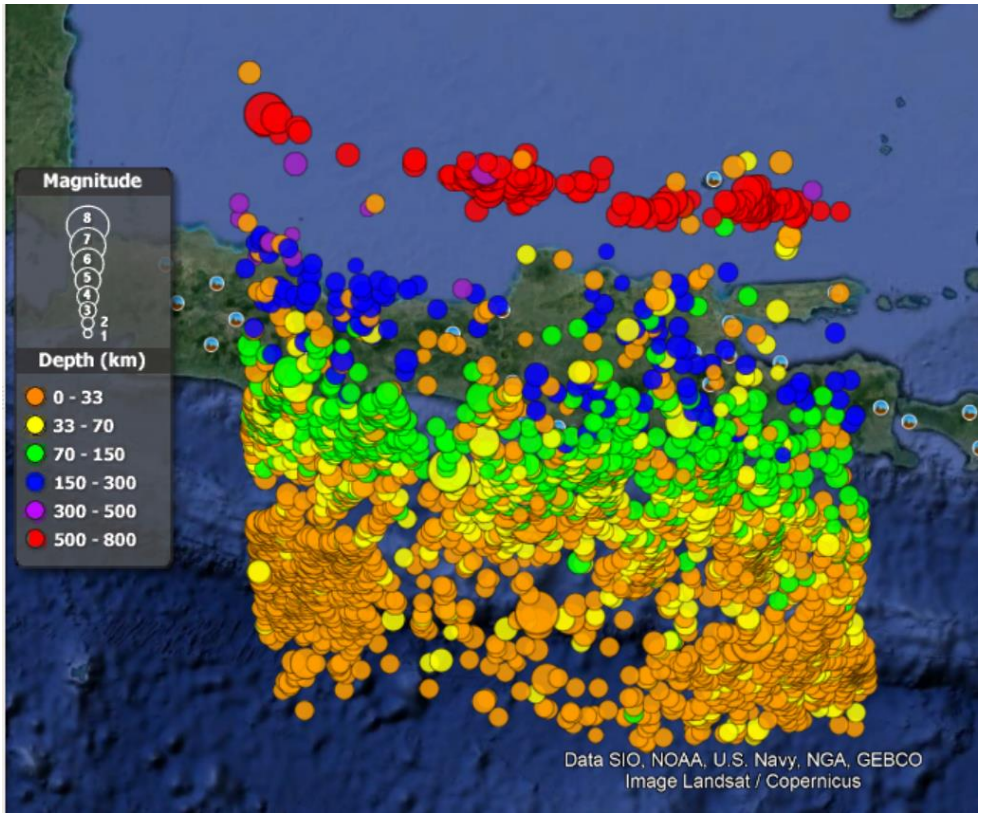


**Supplemental Figure S2:** Records of earthquake occurrences in the Java Sea close to the study site (from https://www.usgs.gov/programs/earthquake-hazards/earthquakes

### 3. Information on modern RSL change in the region

Modern changes in relative sea level near Jepara are associated to El Nino Southern Oscillation (e.g. 1997 and 2011) and Southern Oscillation Index. With amplitudes of less than 0,2 m, the annual sea level variations are small, but may in some years be double or more (Supplemental Figure S3).

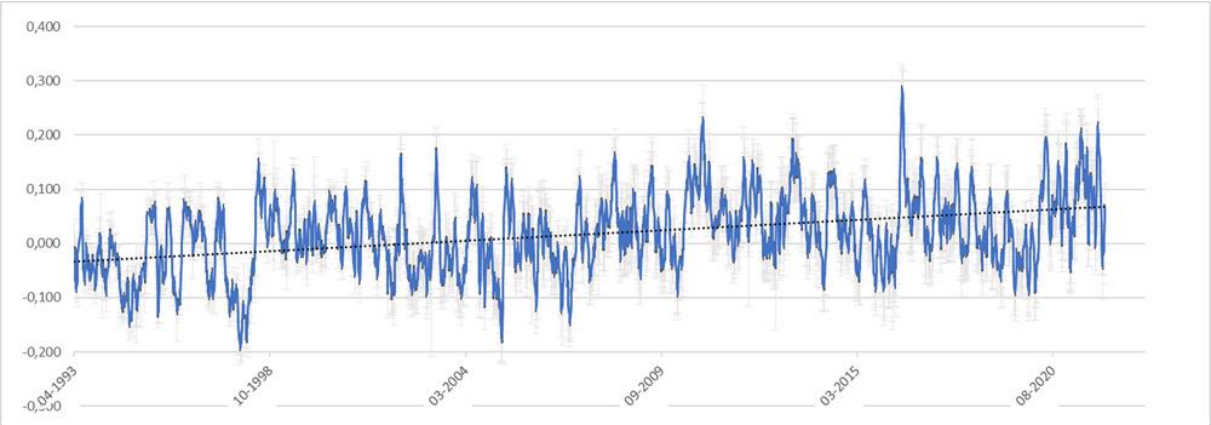


**Supplemental Figure S3:** Sea level curve near Jepara derived from a combination of Topex & Jason-1 to Jason-3 radar altimetry for 1993 to 2022. The data are derived from GFZ's ADS repository (adsc.gfz-potsdam.de)

### 4. Information on living microatolls within the tidal cycle

Living microatolls occupy an elevational range of 0.53 m around the study site. Supplemental Figure S4 indicates the range with respect to the tidal cycle from the OSU model (Egbert and Erofeeva, 2002).

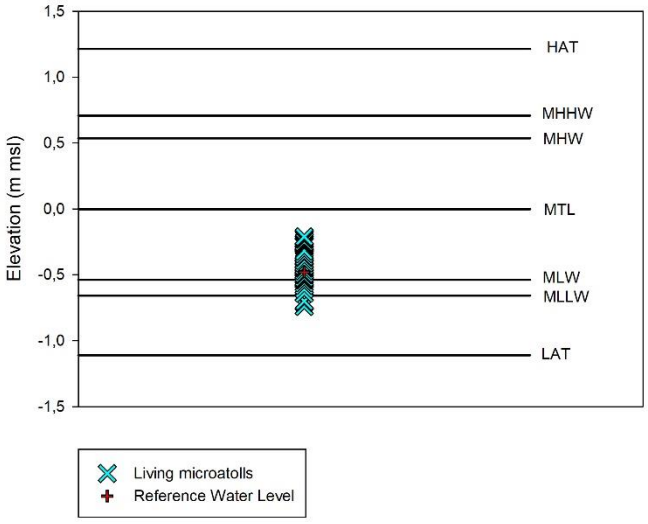


**Supplemental Figure S4:** Elevational range of living microatolls with respect to the tidal frame modelled by Egbert and Erofeeva (2002).

## 5. Morphological Information on RSL indicators categorized as fossil microatolls

Supplemental Figure S5 shows all RSL indicators that have been categorized as fossil microatolls in the present study. Below is a short description on the dimensions and appearance of all analyzed fossil microatolls.

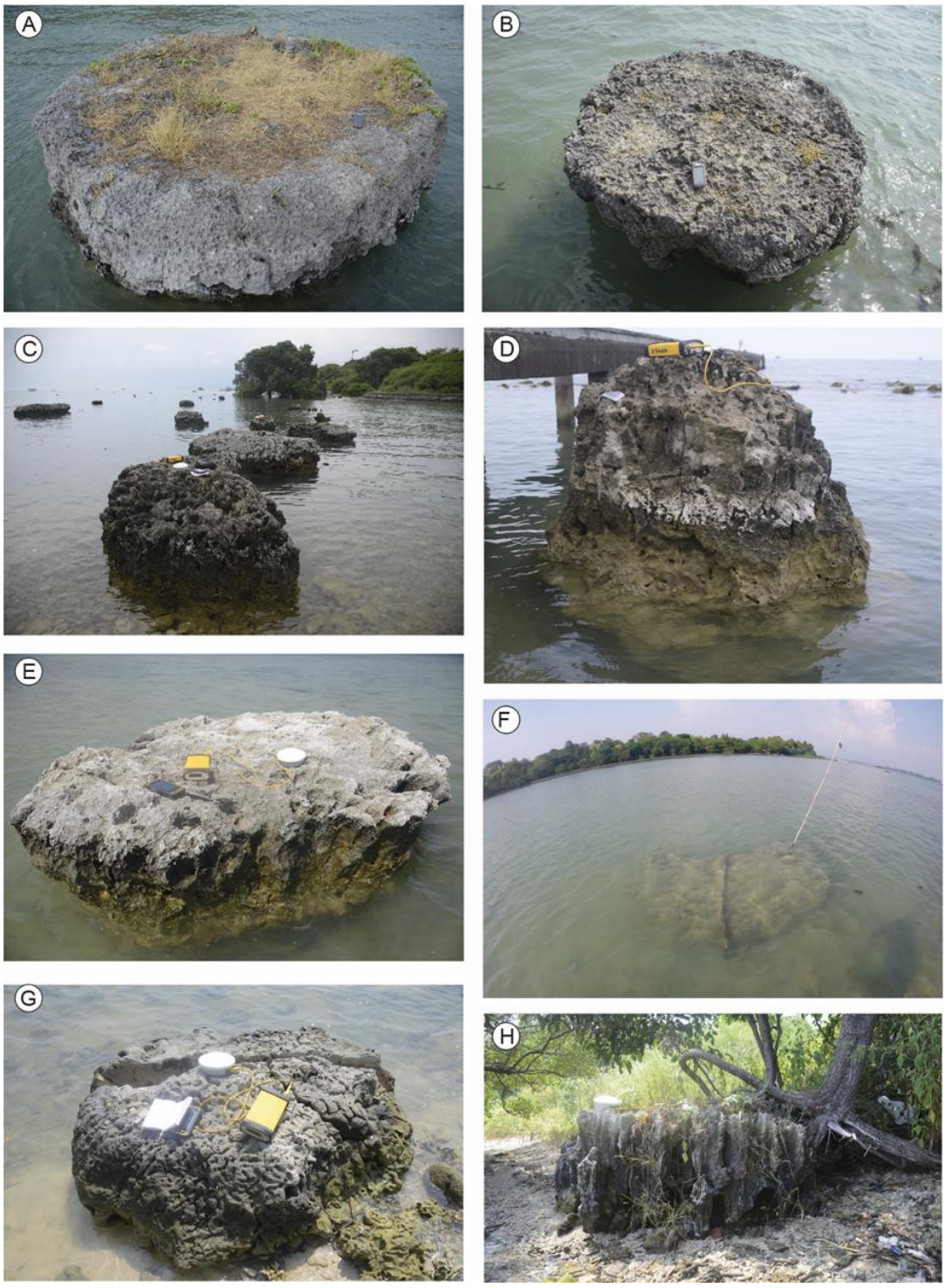


**Supplemental Figure S5**: Field geomorphological characteristics and full-frame photographs of RSL indicators categorized as fossil microatolls.

PPJ_FMA1 (Supplemental Figure S5A):

This specimen is the largest of all analyzed microatolls with heights above the reef flat between 1.65 m at the southern side and 1.9 m at the western side. The top diameter ranges between 3.78 m in a E-W section and 4.3 m in a NNW-SSE section. The surface is near horizontal with saucer morphology. The coral is heavily notched at the base.

PPJ_FMA2 (Supplemental Figure S5B):

This specimen is 1 m seaward of PPJ_FMA1 and approximately half the size. The lithology is similarly a homogenous grey carbonate rock with slightly karstified surfaces. Heights above the reef flat range between 1.79 m at the eastern side and 1.84 m at the northern side. The diameter ranges between 2.31 m in a N-S direction and 2.40 m in a E-W direction. The surface is horizontal with remnants of concentric rings. The sides are severely undercut.

PPJ_FMA3 (Supplemental Figure S5C):

This specimen forms the seaward end of a sequence of three fossil microatolls located 100 m north of PPJ_FMA1. It is partly surrounded by the rubble sheet. The heights range from 0.6 m above the rubble rampart at the northern side and 1.5 m above the reef flat at the southern side. The width is 1.7 m in a N-S direction and 2.95 m in a E-W direction. The southern half appears to be eroded.

PPJ_FMA4 (Supplemental Figure S5C):

This specimen is located in the center of the sequence, approximately 2 m distant from the toe of the rubble sheet slope. The surface is well-cemented and near horizontal with a slight slope along its N-S axis (lower to N). Elevations above the reef surface between 1.2 m and 1.4 m at all sides and the diameter ranges between 2.54 m along a N-S transect and 2.7 m along its E-W section.

PPJ_FMA5 (Supplemental Figure S5C):

This specimen forms the landward end of the triple sequence and is partly broken off on the seaward western side. The heights account for ~1.15 m above the reef flat at all sides and the diameter is 1.7 m except for the E-W axis with the broken off segment.

PPJ_FMA6 (Supplemental Figure S5D):

This specimen is heavily notched and eroded along the sides as the base is considerably wider than the top. The heights above the reef crest range between 1.64 m and 1.80 m. The diameter at the base of the coral is between 1.7m and 2m whereas the diameter at the upper section is between 1 m and 1.3 m.

PPJ_FMA7 (Supplemental Figure S5E):

This specimen rests on a sand flat about 30m behind the rubble rampart. The diameter is between 2.49 m along the N-S axis and 2.19 m along the E-W axis. Heights above the sand flat range between 1.2 m at the northern side and 1.02 m at the eastern side. The surface is near horizontal and characterized by a saucer morphology with a ~0.15 m relief from the outer rim to the center.

PPJ_FMA8 (Supplemental Figure S5F):

This specimen represent the remnants of a discoidal coral with a planar surface. The landward 1/3 of the fossil microatoll is missing. The diameter ranges between 1.11 m along the short axis and 2.5 m along the long axis. The elevation ranges between 0.28 m and 0.35 m above the sand flat.

PPJ_FMA9 (Supplemental Figure S5G):

This specimen is located at the NW shoreline of Pulau Panjang, approximately 1.7 m wide and 0.7 m above the sand / gravel surface. The surface is relatively horizontal and significant erosion is not observable. It is possible that the coral had been buried by the island and only recently been exhumed.

PPJ_FMA10 (Supplemental Figure S5H):

This specimen is located onshore and approximately 2.2 m in diameter. The surface is horizontal and the highest elevation above the sand / gravel is 0.8 m. Similarly to PPJ_FMA9, significant erosion has likely been prevented by burial by the island.

## 6. Morphological Information on RSL indicators categorized as marine limiting data

Supplemental Figure S6 shows all specimens that have been categorized as marine limiting data in the present study. Below is a short description on the dimensions and appearance of each marine limiting data point.


**Supplemental Figure S6:** Full-frame photographs of RSL indicators categorized as marine limiting data

PPJ CB1 (Supplemental Figure S6A):

This specimen has an irregular and non-horizontal surface, is 1.17 m elevated above the reef flat and between 1.2 m and 1.3 m wide in the top section. The side walls are partly notched.

PPJ CB2 (Supplemental Figure S6B):

This specimen is heavily undercut by tides and shows a strongly inclined and irregular surface. The highest point of the coral is 1.23 m above the reef flat. In the top section, the specimen is between 0.7 m and 0.5 m wide.

PPJ CB3 (Supplemental Figure S6C):

This specimen shows an irregular morphology, is 1.57 m wide at the longest axis, and between 0.83 m and 0.46 m at the short axis. The highest point is 0.86 m above the reef flat.

PPJ CB4 (Supplemental Figure S6D):

This specimen shows again strong undercutting at the side walls and the highest point is approximately 0.68 m above the reef flat. The surface is highly uneven and the diameter is between 0.67 m and 0.52 m.

## 7. Survey information and msl calculation

All elevations have been measured using a Trimble proXRT receiver with Tornado Antenna and Juno ST data collector with Terrasync software, connected to a real-time satellite differential correction Omnistar HP subscription. Each relative sea-level indicator has been measured for at least 30 minutes in order to achieve a high vertical precession in the elevation measurements. Transect waypoints used to reconstruct the reef flat geomorphology have been surveyed for a duration of approximately 5 minutes for each point.

In order to benchmark the GPS data to a local tidal datum, we determined the vertical difference between the ellipsoid and local mean sea level (msl) retrieved from water-level measurements at (i) the study site, (ii) the Tide Gauge station in Jepara, (iii) the actual tide gauge data from the station in Jepara, (iv) mean sea surface height models and (v) satellite altimetry data. We deployed two pressure sensor loggers both at the site of fieldwork (Pulau Panjang) and at the Tide Gauge station in Jepara, which lies approximately 2 km east-southeast of Pulau Panjang, for the duration of fieldwork. At each site, one logger was deployed below low tide levels and the other logger was deployed on land. Elevations of the “under-water” logger sensors have been surveyed with the RTK GPS system as well.

Accordingly, at each site one logger captured both water and air pressure (i.e. the one deployed under water) and the other logger recorded barometric pressure changes (i.e. the one deployed on land). Water levels (in m) above those loggers deployed under water have been calculated by subtracting the air pressure (in mbar) from the absolute pressure (in mbar) at each time step, and then multiply the remaining pure water pressure (in mbar) with the constant 0.010197162 (i.e. 1mm H2O = 0.0980665 mbar).

Results showed that the Tide Gauge station in Jepara measured water levels at 0.08±0.05 m (2σ) below our water level logger at that station. Furthermore, our water level logger on Pulau Panjang was deployed 0.05±0.05 m (2σ) below our water level logger at Jepara. Vertical errors result from the comparison of water levels at each time step between (i) tide

gauge measurements and logger data at Jepara (n=120), and between (ii) logger data at Jepara and logger data on Pulau Panjang (n=7141).

Tide gauge data from the station at Jepara (1 January 2014 – 1 June 2016) indicate that msl is at 0.931 m, which would result in a msl relative to our water level logger at Jepara at 0.901±0.05 m (2σ). However, during this comparably short time span, msl calculated from different public mean sea surface height models (CL11; DT15; CL01; GS00) and combined radar altimetry (TOPR, ENVI, JASE, J2_D, J3_T, ALTK, CR2A) is 0.14 m above the altimetry long-term time series (April 1994 – February 2017). Accordingly, we subtracted this value from the short-term msl derived from the Tide Gauge station in Jepara (0.931 m) and referred our GPS surveys to a long-term (> 19 years) msl of 0.76±0.12 m (2σ) above our water level logger at the study site. Vertical errors comprise uncertainties from the comparison of logger elevations (see above) and the vertical error of the RTK GPS Logger position at Pulau Panjang (0.096m).

## 8. Discussion of uncertainties in the proxy elevations

When we determined the uncertainties regarding the elevations of microatoll surfaces, we considered (i) sampling uncertainties, (ii) survey uncertainties related to the RTK GPS, (iii) benchmark uncertainties related to the comparison of logger heights and (iv) uncertainties related to the potential meteoric dissolution of coral surfaces (Supplementary Table S1).

Surfaces of fossil microatolls may experience substantial post-mortem abrasion from littoral sediment transport, which must be accounted for in RSL reconstructions (Kench et al., 2009; Mann et al., 2016; Bender et al., 2020). Extensive physical abrasion of microatolls analyzed in this study is unlikely because affected specimens would typically comprise smooth surfaces. However, the undulatory karst morphology of some specimens indicate that meteoric dissolution of the aragonitic coral skeletons is a potential agent of downward erosion.

While there is evidence for punctual dissolution in the form of cavernous solution holes and crevices, experimental results suggest that rates of planar chemical carbonate erosion are minimal and range between 6 – 10 µm yr-1 (Baedecker et al., 1992). Although rates will vary depending on environmental parameters, a conservatively estimated downward surface dissolution of < 0.1 m is in accordance to observed saucer morphologies and remnants of concentric rings on the analyzed microatoll surfaces. In order to account for the potential downward surface dissolution, we have therefore added an error of 0.1 m in the levelling uncertainty of each proxy elevation.

## 9. Slabbing techniques and processing information

Microatoll slabbing was done according to the methodological descriptions provided by Meltzner and Woodroffe (2015). PPJ_FMA9 has been completely slabbed using a two-handled handsaw whereas specimens PPJ_FMA1 and PPJ_FMA2 were partly slabbed (i.e. the outer ~0.7m) with a fuel-driven chainsaw. Before slabbing, the chosen diameter has been tied into the overall survey with screws that were placed along the chosen parts to reconstruct the line of horizontality and its relation to msl after the slab had been removed. Before the slabs were packed in wooden boxes for transport, small holes along the line of horizontality have been drilled into the slab for later identification in x-ray images. The slabs have been sliced to an approximate thickness of 10 mm at a construction company and were afterwards x-rayed at the Center for Modern Diagnostics (ZEMODI) in Bremen.

**10. Information on the reconstruction of slab chronologies**

For specimen PPJ_FMA9, weighted averages of $^{14}C$ dates from seven sub-samples from various growth bands on the microatoll slabs have been determined according to the methods described in Meltzner and Woodroffe (2015) and Meltzner et al. (2017). In doing so, we used the D_Sequence () function in OxCal, where the known time that has lapsed between two measurements is incorporated. For the determination of the weighted average age of the outer band of slab PPJ_FMA9, we only used the radiocarbon dates from sub-samples PPJ_FMA9, PPJ_FMA9_RC8, PPJ_FMA9_RC9 and PPJ_FMA9_RC10 as the x-ray image revealed that this fossil microatoll comprises two individuals that have coalesced.

For specimens PPJ_FMA1 and PPJ_FMA2 only partial slabs could have been removed. In order to determine weighted averages of $^{14}C$ dates for specimens PPJ_FMA1 and PPJ_FMA2, we have included two sub-samples from each slab where individual growth bands are visible. Supplemental Table S2 shows detailed parameters for the determination of the modelled age of the outer band.

**Supplemental Table S2:** Results from the D_Sequence analysis in OxCal

| Name | Unmodelled (2 sigma, BP) | | | | No. of younger annual bands | Unmodeled age of outer band | Modelled (2 sigma, BP) | | | |
|---|---|---|---|---|---|---|---|---|---|---|
| | from | to | median | 2 sigma uncertainty | | | from | to | median | 2 sigma uncertainty |
| R_Date PPJ_FMA1 | 6758 | 6407 | 6586 | 175,5 | 69 | 6517 | 6622 | 6412 | 6511 | 105 |
| R_Date PPJ_FMA1_RC1 | 6607 | 6279 | 6433 | 164 | 42 | 6391 | 6595 | 6385 | 6484 | 105 |
| R_Date PPJ_FMA1_RC2 | 6625 | 6293 | 6455 | 166 | 25 | 6430 | 6578 | 6368 | 6467 | 105 |
| **PPJ_FMA1_outer band** | | | | | | | | | **6442** | **105** |
| R_Date PPJ_FMA2 | 6736 | 6392 | 6564 | 172 | 43 | 6521 | 6668 | 6468 | 6568 | 100 |
| R_Date PPJ_FMA2_RC3 | 6691 | 6345 | 6518 | 173 | 31 | 6487 | 6656 | 6456 | 6556 | 100 |
| R_Date PPJ_FMA2_RC4 | 6758 | 6408 | 6583 | 175 | 18 | 6565 | 6643 | 6443 | 6543 | 100 |
| **PPJ_FMA2_outer band** | | | | | | | | | **6525** | **100** |
| R_Date PPJ_FMA9 | 6736 | 6392 | 6564 | 172 | 40 | 6524 | 6699 | 6517 | 6614 | 91 |
| R_Date PPJ_FMA9_RC8 | 6774 | 6421 | 6598 | 176,5 | 28 | 6570 | 6687 | 6505 | 6602 | 91 |
| R_Date PPJ_FMA9_RC9 | 6838 | 6476 | 6656 | 181 | 24 | 6632 | 6683 | 6501 | 6598 | 91 |
| R_Date PPJ_FMA9_RC10 | 6751 | 6411 | 6586 | 170 | 19 | 6567 | 6678 | 6496 | 6593 | 91 |
| **PPJ_FMA9_outer band** | | | | | | | | | **6574** | **91** |

## 11. Information on isostatic modeling

We use a nominal ice model (43c_20_17_12) that includes the northern hemisphere ice sheets, an Antarctic ice sheet, and mountain glaciers in both hemispheres. The corresponding ice-volume function (or ice-volume equivalent sea level) has been presented in Lambeck et al. (2014). We combined the ice model with the t2E far-field continental margin model (Lambeck et al., 2014) that is based on sea-level data inversion from SE Asia, including Singapore (Bird et al., 2007; Bird et al., 2010) and the Sunda Shelf (Hanebuth et al., 2000). The predicted distinctive regional pattern in sea-level change for the Malay-Indonesian Archipelago based on changing surface load, notably the water load, is shown in supplemental Figure S7.

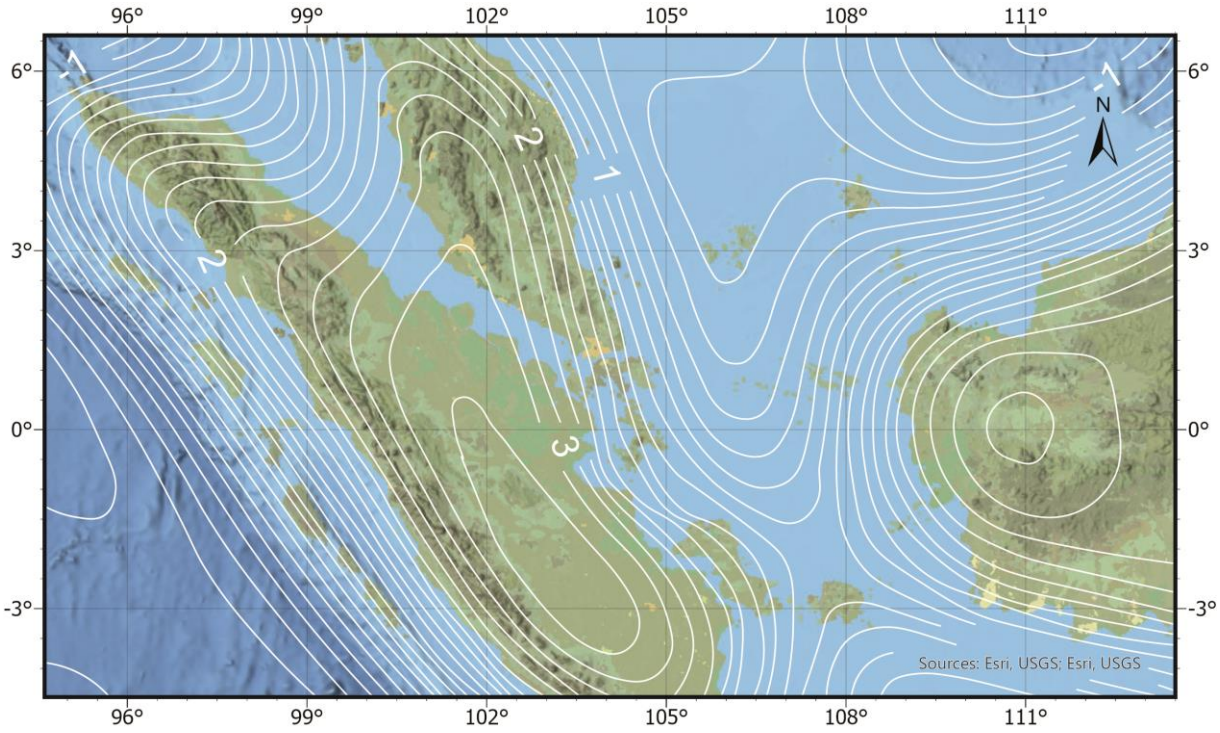


**Supplemental Figure S7**: Contours of the predicted relative sea level change at 6000 years ago for part of the Malay-Indonesia Archipelago based on the three-layer GIA and ice parameters discussed in text. Contours at 25 cm interval with upper values of ~3m predicted for the central part of the Strait of Malacca and lower of ~ 0 for the Anambas Islands in the North Natuna Sea.

We have used here the 3-layer earth-model parameters (Supplemental Table S3) based on inversions of a global data set of far-field rsl data back to Marine Isotope Stage 5, loaded by ice-sheet models that have been constrained by geological data and from regional rebound analysis of the formerly glaciated regions and the constraint that the global ice-mass change is conserved throughout (Lambeck et al., 2014). These solutions differ in a minor way from Lambeck et al., 2014 in that they represent a further iteration in which the corrective for the ice-volume equivalent sea level correction has been redistributed between the ice sheets followed by a new parameter search.

**Supplemental Table S3:** Effective viscosity estimates for representative three-, four- and five-layered models based on inversion of far-field rsl data. *H* refers to the effective elastic thickness of the lithosphere; UM to the mantle viscosity above the 670 km seismic discontinuity, LM to the lower mantle down to the core-mantle boundary (CMB), IM to the intermediate mantle from 670 km depth to the CMB. The last two columns give the 95% confidence limits of the solution parameters.

| | | Solution | Confidence limits | |
|---|---|---|---|---|
| | | | lower | upper |
| 3-layer mantle | $\psi^2$ min | 3.23 | | |
| | H (km) | 63 | 45 | 80 |
| | UM (H to 670 km)(x $10^{20}$ Pa s) | 1.8 | 1.5 | 2.5 |
| | LM (670 km to CMB)(x $10^{22}$ Pa s) | 4.8 | 1.7 | >20 |
| 4-layer mantle | $\psi^2$ min | 3.27 | | |
| | H (km) | 60 | 40 | 90 |
| | UM (H to 670 km)(x $10^{20}$ Pa s) | 1.8 | 1.3 | 3 |
| | IM (670 to 1200 km)(x $10^{22}$ Pa s) | 10 | 2.6 | >20 |
| | LM (1200 km to CMB)(x $10^{22}$ Pa s) | 4.3 | 2.3 | >20 |
| 5-layer mantle | $\psi^2$ min | 3.71 | | |
| | H (km) | 55 | 40 | 90 |
| | UM-1 (H to 200 km)(x $10^{20}$ Pa s) | 1.75 | 1.5 | 3 |
| | UM-2 (200 to 400 km)(x $10^{20}$ Pa s) | 1.75 | | |
| | UM-3 (400 to 670 km)(x $10^{22}$ Pa s) | 1.75 | | |
| | LM (670 km to CMB) set at 1.5 x $10^{22}$ Pa s | 1.5 | | |

Regional inversions of data sets for more complex layering yield statistically equivalent solutions (Supplemental Table S3): for example, introducing the potential for viscosity boundaries at either 200 and/or 400 km depth yield near identical viscosities ( e.g. the 5-layer model); nor is there compelling evidence for lower mantle layering (e.g. the 4-layer solution), inferences that are supported by inversions for the major ice-sheet mantle model parameters (Lambeck et al., 2017). Thus, while the models provide good descriptions of the Earth-ocean regional response to the changing ice loads – with the proviso that the effective mantle parameters are regionally variable – this result does not imply that the actual radial-variation of viscosity is so simple, but that more detailed depth-dependence is not essential for providing a predictive capability that is consistent with the accuracies of available rsl and ice-sheet observational evidence.

Supplemental Figure S8 illustrates a part of the searched 3-dimensional parameter space $\psi^2$ for two sections (H – $\eta_{um}$ for $\eta_{lm}$ = 5 x $10^{22}$ Pa s and $\eta_{lm}$ – $\eta_{um}$ for H = 60 km) with the two planes intersecting at the least-variance solution whose 95% confidence limits correspond approximately to the 3.5 contours. Of the three parameters, the upper-mantle effective viscosity is well resolved at (1.5 – 2.5)$10^{20}$ Pa s. Resolution for lithospheric thickness is less satisfactory with values less than ~30 km or greater than ~100 km excluded. Improved solutions for this parameter will require more accurate rsl data across the margins, and a closer examination of potential sites in the Malay-Indonesian Archipelago for which considerable spatial variability in predicted rsl for the last 6000 – 7000 year is warranted.

The lower-mantle $\eta_{lm}$ is least well resolved – reflecting the relative insensitivity of this zone to the load changes – and two local minima are identified – a low $\eta_{lm}$ of ~ 3x$10^{22}$ with $\psi^2_{min}$ = 3.23 and high $\eta_{lm}$ ~5x$10^{22}$ Pa s with $\psi^2_{min}$ = 3.73. However, the latter value lies outside the confidence limits of the former and is also excluded by the glaciated continental mantle solutions (Lambeck, 2017), accordingly we have adopted the weighted mean of all regional solutions.

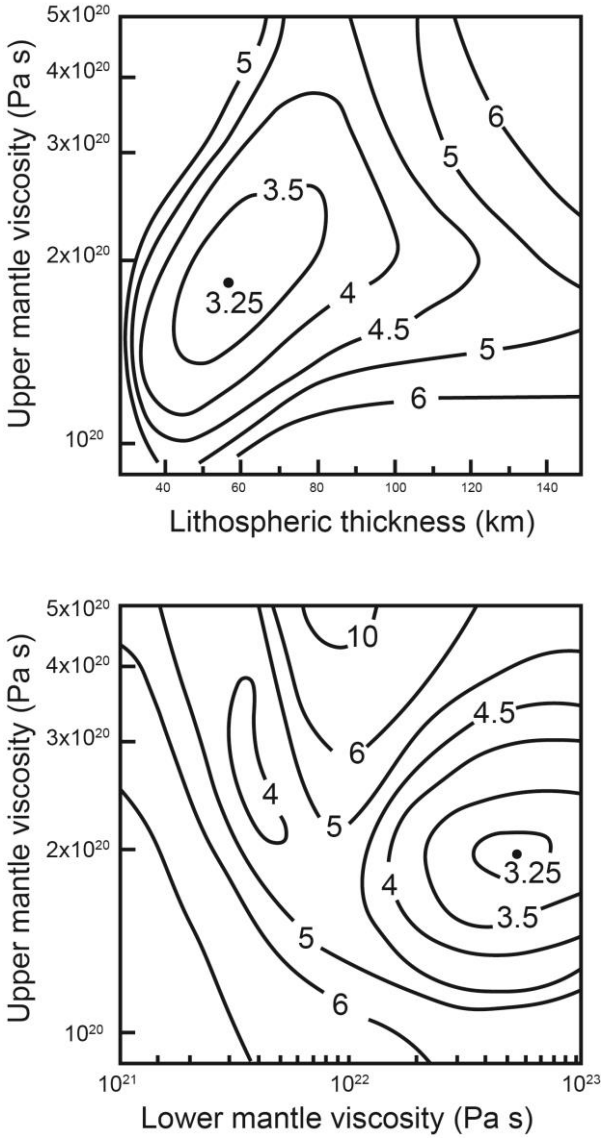


**Supplemental Figure S8:** Two sections through part of the 3-dimensional parameter space of the variance function through the least variance solution $\psi^2_{min}$. Upper, the *H* – $\eta_{um}$ plane for constant lower mantle for $\eta_{lm}$ = 5x$10^{22}$ Pa s and lower, the $\eta_{lm}$ – $\eta_{um}$ plane for =60 km, both planes passing through the least variance value for the three-layer model inversion.

**11. Information on RSL modeling**

RSL data reconstructed from the three microatoll slabs have been statistically evaluated using a hierarchical empirical temporal Gaussian process statistical model (Ashe et al., 2019) similar to the model developed in Meltzner et al. (2017). A number of differences between the two approaches exist; first, we consider the RSL data from the slabs as index points and not as marine limiting data. Even though there is some degree of surface erosion, observable concentric annuli on the surfaces of the slabbed specimens, saucer morphologies and the detection of a “highest level of survival” (HLS) unconformity on slab PPJ_FMA9 show that the meteoric dissolution was only minimal. Furthermore, vertical differences between the highest level of growth (HLG) and HLS is maximal in the range of 0.1m during a tidal cycle when considering the growth rates of the corals and the local tidal system. This vertical uncertainty lies well within our conservative vertical error estimation. Second, we do not fit our RSL curve to a sinusoidal function with a frequency of 18.6 years, as we are not detecting a tidal signal in the data. Third, we do not include spatial differences between sites as all slabs come from the same locality.

**Supplemental References:**

Ashe, E. L., Cahill, N., Hay, C., Khan, N. S., Kemp, A., Engelhart, S. E., Horton, B. P., Parnell, A. C., and Kopp, R. E., 2019, Statistical modeling of rates and trends in Holocene relative sea level: Quaternary Science Reviews, v. 204, p. 58-77.

Baedecker, P. A., Reddy, M. M., Reimann, K. J., and Sciammarella, C. A., 1992, Effects of acidic deposition on the erosion of carbonate stone—experimental results from the US National Acid Precipitation Assessment Program (NAPAP): Atmospheric Environment. Part B. Urban Atmosphere, v. 26, no. 2, p. 147-158.

Bender, M., Mann, T., Stocchi, P., Kneer, D., Schöne, T., Illigner, J., Jompa, J., and Rovere, A., 2020, Late Holocene (0–6 ka) sea-level changes in the Makassar Strait, Indonesia: Climate of the Past, v. 16, no. 4, p. 1187-1205.

Bird, M. I., Austin, W. E., Wurster, C. M., Fifield, L. K., Mojtahid, M., and Sargeant, C., 2010, Punctuated eustatic sea-level rise in the early mid-Holocene: Geology, v. 38, no. 9, p. 803-806.

Bird, M. I., Fifield, L. K., Teh, T., Chang, C., Shirlaw, N., and Lambeck, K., 2007, An inflection in the rate of early mid-Holocene eustatic sea-level rise: A new sea-level curve from Singapore: Estuarine, Coastal and Shelf Science, v. 71, no. 3-4, p. 523-536.

Egbert, G. D., and Erofeeva, S. Y., 2002, Efficient inverse modeling of barotropic ocean tides: Journal of Atmospheric and Oceanic technology, v. 19, no. 2, p. 183-204.

Hanebuth, T., Stattegger, K., and Grootes, P. M., 2000, Rapid flooding of the Sunda Shelf: a late-glacial sea-level record: Science, v. 288, no. 5468, p. 1033-1035.

Kench, P., Smithers, S., McLean, R., and Nichol, S., 2009, Holocene reef growth in the Maldives: evidence of a mid-Holocene sea-level highstand in the central Indian Ocean: Geology, v. 37, no. 5, p. 455-458.

Lambeck, K., Purcell, A., and Zhao, S., 2017, The North American Late Wisconsin ice sheet and mantle viscosity from glacial rebound analyses: Quaternary Science Reviews, v. 158, p. 172-210.

Lambeck, K., Rouby, H., Purcell, A., Sun, Y., and Sambridge, M., 2014, Sea level and global ice volumes from the Last Glacial Maximum to the Holocene: Proceedings of the National Academy of Sciences, v. 111, no. 43, p. 15296-15303.

Mann, T., Bayliss-Smith, T., and Westphal, H., 2016, A geomorphic interpretation of shoreline change rates on reef islands: Journal of Coastal Research, v. 32, no. 3, p. 500-507.

Meltzner, A. J., Switzer, A. D., Horton, B. P., Ashe, E., Qiu, Q., Hill, D. F., Bradley, S. L., Kopp, R. E., Hill, E. M., and Majewski, J. M., 2017, Half-metre sea-level fluctuations

on centennial timescales from mid-Holocene corals of Southeast Asia: Nature communications, v. 8, no. 1, p. 1-16.
Meltzner, A. J., and Woodroffe, C. D., 2015, Coral microatolls: Handbook of Sea-Level Research, p. 125-145.